doi:10.1246/cl.2012.466
Published on the web April 28, 2012

Highlight Review

Collective Interactions of Molecules with an Interfacial Solid

Katsumi Kaneko,* Tsutomu Itoh, and Toshihiko Fujimori

(Received March 13, 2012; CL-120213)

Abstract

Confinement of molecules in nanoscale pores of an interfacial solid such as single wall carbon nanotubes of which all component carbon atoms are exposed to the interface with gas phase induces collective phenomena; the confinement effect is interpreted by the interaction potential theory. The nanoconfinement effect gives rise to in-pore phase anomalies for NO, H_2O, CCl_4, superhigh-pressure effect, hydrophobic to hydrophilic transformation for carbon, and a marked quantum molecular sieving. The confinement of KI in the nanotube space below 0.1 MPa produces high-pressure-phase KI above 1.9 GPa. Water molecules gain hydrophilicity with cluster formation in order to accommodate in the hydrophobic carbon spaces. The subnanometer quantum fluctuation for H_2 and D_2 gives rise to a marked quantum molecular sieving effect in nanoscale pores. The Cu-based porous coordination polymer crystals can detect the surrounding stimuli such as CO_2 pressure change to vary the crystal lattice, accompanying gate adsorption.

♦ 1. Introduction

Human society had encountered crucial issues of human sustainability in the past. Scientific and technological innovations could give clues to resolving human issues. Present human society faces serious issues of global warming, energy shortages, food and water shortages, and exhaustion of resources. In particular, a marked decline of low CO_2 emission nuclear energy utilization has just invoked an intensive steering toward development of renewable energies, even though a promising prediction of the latent capacity of shale gases has given enough time to create a renewable energy system. Under these circumstances chemistry has a primary mission to play a key role in construction of future renewable energy.

One promising and powerful candidate for contribution to a future renewable energy economy is a nanoporous solid. Nanoporous solids have nanopores whose width w is less than 100 nm. IUPAC recommends using the terminology micropore ($w < 2$ nm), mesopore ($2\,\text{nm} < w < 50\,\text{nm}$), and macropore ($w > 50$ nm). In particular micropores and small mesopores ($w < 5$ nm) can contribute to construction of future renewable energy generation. In this article, we refer to these pores as nanoscale pores. Nanoporous solids are classified into crystalline and noncrystalline solids; zeolites and microporous carbons are representatives of crystalline and noncrystalline porous solids, respectively. These traditional microporous solids have been developed by addition of mesopores to accelerate pore diffusion.[1,2] Fortunately, we have seen an exciting rush exploiting novel nanoporous solid since 1990.[3] Mesoporous silica and carbon nanotubes have stimulated chemistry very much. Mesoporous silicas, of which wall and pore structures are noncrystalline and highly ordered, respectively, have become widespread in chemistry owing to the scalable synthesis. On the contrary, development of the scalable synthesis of high quality single wall carbon nanotubes (SWCNT) has been delayed since the first observation by high-resolution transmission electron microscopy in 1993. Therefore, SWCNT have not been common in chemistry compared to mesoporous silica of which studies have been predominantly conducted in Japan.[4] Iijima et al. succeeded in producing single wall carbon nanohorns (SWCNH), abundantly enabling chemical research since 1999.[5] SWCNH have been studied in chemistry, although the graphene-wall structure and the morphology are more defective and more complex than SWCNT. Recently chemical study even on SWCNT has been possible due to exploitation of supergrowth (SG) SWCNT by Hata et al.[6]

Thus, chemistry has two promising candidates for nanopore-related technologies. Furthermore, porous coordination polymers (PCP) or metal organic frameworks (MOF) have appeared on the science stage after mesoporous silica and carbon nanotubes. PCP of outstanding designability, structural diversity, and huge nanoporosity, have attracted great interest from chemists and engineers, leading to a rapid growth in chemistry.[7–10]

Thus, we have three new giants of mesoporous silica, carbon nanotube, and PCP in the nanoporous world of science and technology. We can allot these new entities to appropriate applications in addition to zeolites and porous carbons, and other porous solids. These nanoporous solids have large surface area and thereby can greatly contribute to construction of the future renewable energy technologies from the aspect of surface chemistry.

SWCNT has 2630 $m^2\,g^{-1}$ of surface area, and all component carbon atoms are exposed to the internal and external surfaces. The two surfaces have different properties depending on the interaction potential, and the internal tube space can have intrinsic functions. Furthermore, SWCNTs can form bundles of hexagonal symmetry, which has interstitial pores and groove sites on the external surfaces. Thus, all carbon atoms in SWCNT can contribute to different surface chemistry originating from a variety of nanostructures. All carbon atoms in double wall carbon nanotubes (DWCNT) can contribute to the surface processes as well.[11] Hence SWCNT and DWCNT can be described as "**Interfacial solid**" or "**Surface solid**." Interfacial solids having nanoscale pores could lead to highly efficient and novel surface chemistry. Activated carbon fiber (ACF) with slit-shaped pores has a huge surface area of 2000–3000 $m^2\,g^{-1}$, and

Prof. Katsumi Kaneko, Dr. Tsutomu Itoh, and Dr. Toshihiko Fujimori*
Research Center for Exotic Nanocarbons, Shinshu University, 4-17-1 Wakasato, Nagano 380-8553
E-mail: kkaneko@shinshu-u.ac.jp

thereby ACF has the nature of the interfacial solid. On this point, PCP has also great possibility. As PCP has a pillar-frame pore structure and the pillar is one-dimensional, the component atoms in the pillars of PCP can interact with molecules in the omnidirection. PCP can be thought of as the interfacial solid, although transition-metal atoms at the junctions of the pillars cannot fully associate with the surface processes.

We can expect unusual molecular or ionic behavior from the interfacial solids. The interfacial solids have nanoscale pores of an intensive interaction potential for molecules and ions, inducing a predominant adsorption on the pore surface. As the total molecular energy in the adsorbed layer can influence the entire energy including the cohesive energy of the interfacial solid, the structure of the interfacial solid may be sensitive to adsorption of molecules and ions. In this article, stabilization effect of an unstable phase, superhigh-pressure effect, a solid structural change sensitive to adsorption, affinity change of water, and filling of molecular quanta are introduced.

♦ 2. Deep Interaction Potential Wells

SWCNT has a rolled graphene structure of which atomic density is 38.2 atom nm^{-2}, being very high. Therefore, the attractive interaction of the graphene structure with a molecule through dispersion interaction is considerably strong. Figure 1 shows a high-resolution transmission electron microscopic image of SWCNT produced by laser ablation, showing a bundle of well-crystalline SWCNTs. The crystallinity of SWCNT can be evaluated by the intensity ratio of G-band (I_G) against D-band (I_D). This SWCNT has a large I_G/I_D ratio over 100. In the case of SWCNT, the tube diameter d in nm and the radial breathing mode (RBM) vibration frequency w in cm^{-1} of Raman spectrum below 800 cm^{-1} is correlated through $d = 248/w$, although we need to measure Raman spectra with different kinds of laser.[12] This highly crystalline SWCNT has a uniform cylinder structure, and then the interaction potential of SWCNT with a molecule in the tube space can be obtained using analytical potential functions.[13]

Figure 2 shows the interaction potential profile between SWCNT and a CH_4 molecule along A–B line. Here SWCNTs form a bundle of hexagonal symmetry. The diameter of SWCNT is assumed to be 1.356 nm; hence, the diameter of the effective tube space is about 1.0 nm. As the spherical size of the CH_4 molecule is 0.381 nm, CH_4 molecules are adsorbed only in the internal tube spaces, whereas they are not in the interstitial space, where the interaction potential is repulsive. Although the interstitial space can give the deepest interaction potential well for a smaller molecule, entrance blocking perturbs the complete filling. We need expand the intertube distance to utilize the interstitial porosity, pillaring of C_{60} increases the interstitial porosity to give better H_2 adsorptivity.[14] On the other hand, a groove site surrounded by two SWCNTs gives the deepest interaction potential. There are two deep potential wells—monolayer position on the internal tube wall and groove position—in this bundle. The potential depth is close to 2000 Kk_B, being much larger than the thermal energy at room temperature (ca. 300 K). Consequently, molecules tend to drop in these deep potential wells in the SWCNT bundles. That is, molecules tend to be adsorbed in the internal tube space and on the groove sites as much as possible, being governed by

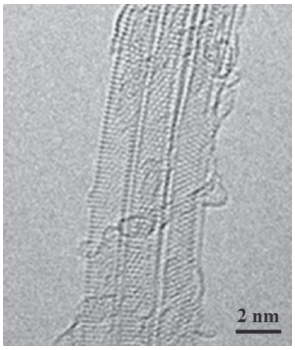

Figure 1. SWCNT image with high-resolution transmission electron microscopy (HR-TEM).

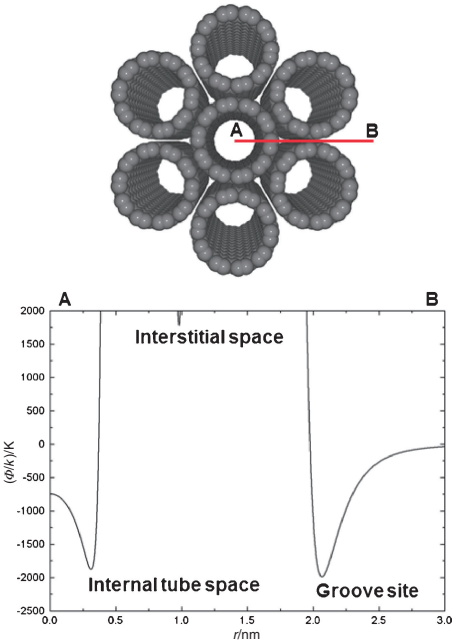

Figure 2. Interaction potential profile between SWCNT bundle and a CH_4 molecule along A–B line in the bundle model. The diameter of SWCNT is 1.356 nm.

statistical mechanics. A system of gases and mesoporous solids can gain significant stability regardless of the decrease of the entropy term, giving rise to novel nanoconfinement phenomena given below. Here we need to pay attention to distinct differences in the potential wells of the internal tube space and the groove site. The potential well in the internal tube space is physically surrounded by the carbon wall, whereas the potential well originating from the groove structure is not physically surrounded. The potential well at the groove has open accessibility to molecules in the gas phase. Consequently, no kinetically limited adsorption occurs at the groove sites of the open access potential wells. On the contrary, molecules must diffuse in the pore spaces to be settled in the potential well in the internal tube space. When the intrapore diffusion of molecules is slow, pore entrance blocking becomes predominant to induce imperfect filling.

♦ 3. Collective Interactions in Pore Space

Interfacial solids of nanoscale pores can offer a collective adsorption in the nanoscale pores of the deep interaction potential well. As abundant molecules confined in the nanoscale pores is comparable to the component atom number of the interfacial solid, credible information on molecules hidden in the pores can be obtained with the aid of X-ray, neutron, and spectroscopic methods. Molecular simulation can have a complementary role in understanding of molecules confined in the pore spaces. We introduce representatives of unique collective interactions between molecules and pores here.

3.1 In-pore Phase Anomaly.

An NO molecule has an unpaired electron and NO gas exhibits paramagnetism. NO molecules are dimerized in the condensed phase below 121 K, showing diamagnetism.[15] Hence, the magnetism directly provides the association state of NO molecules. NO molecules are not sufficiently adsorbed even in nanoscale pores at an ambient temperature, because the critical temperature of NO is 180 K. However, modification of ACFs with nano iron oxides enhances dimerization of NO, leading to an incredibly large adsorption of more than 300 mg g^{-1} at 303 K. It was found that NO molecules are adsorbed in the dimerized form in micropores of ACF and zeolites at 303 K with the aid of magnetic susceptibility measurement. The NO dimers are stabilized; the excess stabilization energies are 1–18 kJ mol^{-1} in the zeolite and 13–15 kJ mol^{-1} in ACF.[16–18] Therefore, confinement of NO molecules in micropores at 303 K stabilizes the NO dimer which is stable below the boiling point (121 K) in the bulk phase. Similar stabilization of the NO dimer is evidenced for SWCNT by Yates et al.[19] The NO stabilization in micropores clearly indicates that the in-pore phase is different from the bulk phase at the same temperature.

CCl_4 crystallizes at 250 K as a plastic crystalline face-centered cubic structure and undergoes a transition to an ordered monoclinic form below 226 K in the bulk.[20] Here a plastic crystal is defined as a special solid phase having long-range positional order for the center of the molecules, but only short-range orientational order. GCMC simulation and in situ X-ray diffraction studies have shown that the plastic crystal phase is stable in slit-shaped pores of ACF whose width is smaller than 1 nm at 303 K.[21] This indicates the transition temperature of the plastic crystal in the micropores is shifted by 53 K at least. Thus, nanoconfinement induces a marked enhancement of the collective interaction between molecules, stabilizing the low-temperature phase. Miyahara and Gubbins predicted an upward shift of the freezing temperature of molecules strongly interacting with micropores by GCMC simulation.[22] A careful differential scanning calorimetry experiment showed that the melting temperature of benzene confined in the micropores of ACF was in the range of 294–298 K, being higher than that of bulk benzene by 16–20 K and that the enthalpy of fusion is about a half of the bulk.[23] Similar elevation was observed for CCl_4, which was supported by a free energy calculation.[24,25]

Recently, this phase transition anomaly was evidenced by vibration–rotation spectroscopy at low temperature for CH_4 in the pores of SWCNH.[26] CH_4 is the main component of natural gas. The CH_4 has become indispensable to our present society, because CH_4 from shale gas can fulfill natural gas demand for about 100 years. Hence CH_4 storage by adsorption has become an urgent issue, consequently, understanding of CH_4 in nanoscale pores is required. Because SWCNH consists of a defective graphene wall through which infrared light passes, we can measure the vibration spectrum of CH_4 confined in pores of SWCNH to elucidate the molecular motional state of CH_4 in the pore. CH_4 in the gas phase gives vibration–rotation bands providing information on vibration and rotation of the CH_4 molecule. Figure 3 shows the difference spectra of antistretching mode between adsorbed CH_4 and bulk CH_4 above 112 K.[26] The gaseous CH_4 has fine rotational structures of P, Q, and R branches at the boiling point of 112 K. However, the P and R branches of the adsorbed CH_4 at 112 K are nearly absent. Hence, the rotational motion is quenched, indicating the highly packed state of CH_4 molecules in pores. With elevating temperature, the slightly shifted P and R branches appear gradually. The P and R branches become evident at 140 K. Therefore, CH_4 molecules rotate almost freely like gaseous CH_4 at 140 K. The more tightly packed "liquid" structure is then stabilized even above the bulk boiling point. The confinement of CH_4 molecules in the SWCNH pores changes also the enveloping shape of P and R branches, suggesting a change in the average rotational motions.

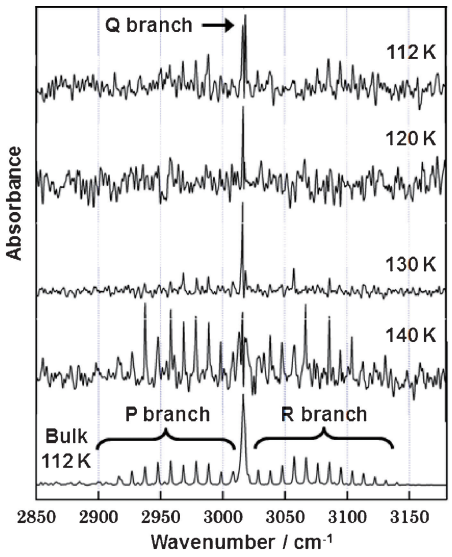

Figure 3. The difference spectra of antistretching mode between adsorbed CH_4 and bulk CH_4 above 112 K.

The molecular level study of nanoconfined molecules has just started, and future studies should provide new insights. Gubbins et al. showed phase anomalies in small pores theoretically.[27] Kanda and Miyahara have attempted to interpret phase anomalies in pores for simple molecules whose interaction can be approximated by the Lennard–Jones potential.[28] Molecular simulation has helped to provide a general understanding for in-pore phase anomalies.

3.2 Superhigh-pressure Effect.

The marked stabilization of NO dimers in micropores is described in Section **3.1**. Highly concentrated NO dimers in micropores induce disproportionation reaction, known as high-pressure gas-phase reaction at 20 MPa, given by eq 1.[29]

$$3(NO)_2 \rightarrow 2N_2O + 2NO_2 \quad (1)$$

As highly concentrated NO dimers in micropores correspond to NO compressed at high pressure, this disproportionation reaction occurs in micropores of ACF below 0.1 MPa at 303 K.[30] Furthermore, the produced N_2O is rapidly reduced to N_2 at 303 K with the aid of dispersed Ru or Pt,[31] although the decomposition of NO to N_2 and O_2 occurs on Cu-ZSM-5 near 750 K.[32] Thus, confinement of reactant molecules in slit-shaped micropores of ACF gives rise to the high-pressure gas-phase reaction. This effect was named quasi-high-pressure effect.[30] Later this high-pressure effect was applied to electrochemical reduction of CO_2 by Fujishima et al.[33] Ordinarily the electrochemical reduction of CO_2 needs compression of CO_2 under about 5 MPa. However, the reaction proceeds under ambient pressure using an ACF electrode.[34] Gubbins et al. gave a theoretical foundation for the high-pressure effect for confinement of molecules in micropores.[35,36]

In the case of cylindrical pores with a deeper interaction potential well than the slit pores, we can expect a more intensive high-pressure effect. As a solid exhibits an inherent phase transition at a definite temperature and pressure, the solid-phase transition can be applied to determine the effective pressure of the high-pressure effect due to the nanoconfinement. KI crystals transform from the B1 phase of NaCl type into B2 phase of CsCl type at 1.9 GPa.[37] The KI structure in the one-dimensional cylindrical space of SWCNT was studied by Meyer et al. with HR-TEM to show anisotropic growth.[38] We doped KI nanocrystals in the tube space of SWCNH of 2–5 nm in diameter at 1073 K below 0.1 MPa.[39] The KI nanocrystals in the tube spaces were examined with HR-TEM and synchrotron X-ray diffraction (XRD) at Spring-8. Figure 4 shows HR-TEM images of the B2-type KI crystals from two directions. The cross-sectional HR-TEM image evidences the formation of KI nanocrystals in the tube space. The predominant contrast comes from iodine atoms in the observed HR-TEM image, because potassium is a light element. The average atomic distances between iodine atoms along the tube axis and perpendicular to the tube axis show that the observed image stems from the *ac* plane of the KI crystal; the direction along the tube axis corresponds to the *c* direction of the crystal, and the direction perpendicular to the tube axis is assigned to be *a* or *b* direction of the crystal. The lattice constants from the HR-TEM image coincide with those of the anisotropic B2 type. Thus, the HR-TEM clearly evidences the formation of high-pressure-phase KI.

Synchrotron XRD firmly supports the formation of the high-pressure-phase KI. Figure 5 shows synchrotron XRD patterns of KI on SWCNH, SWCNH, and bulk KI at room temperature. The XRD pattern of the bulk KI crystals indicates that $a = b = c = 0.7063$ nm and $\alpha = \beta = \gamma = 90°$, agreeing with those of ambient-pressure-phase KI crystals. In the XRD pattern of KI on SWCNH, we observe several peaks which cannot be assigned to the ambient-pressure-phase KI and SWCNH. The detailed analysis showed that these unassigned peaks originated from both the slightly distorted B1- and B2-type structures. The observed B2 (high-pressure phase) structures are slightly distorted from the simple B2 type. The intensive confinements of KI crystals should distort the lattice slightly. Both HR-TEM and synchrotron XRD examination explicitly evidence the growth of the high-pressure-phase KI, indicating that confinement in the tube spaces gives rise to the remarkable compression effect by more than 1.9 GPa.[40]

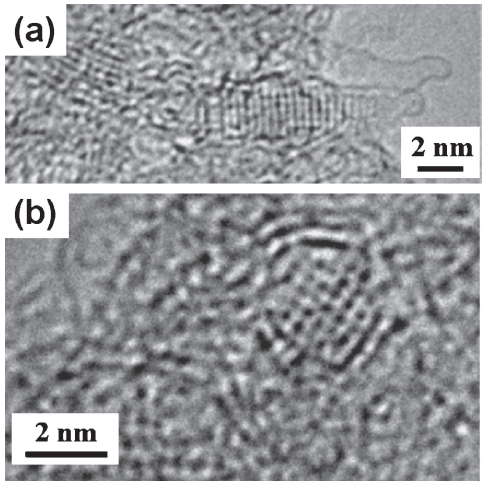

Figure 4. HR-TEM images of the B2-type KI nanocrystals. (a) Along tube direction and (b) cross-sectional image.

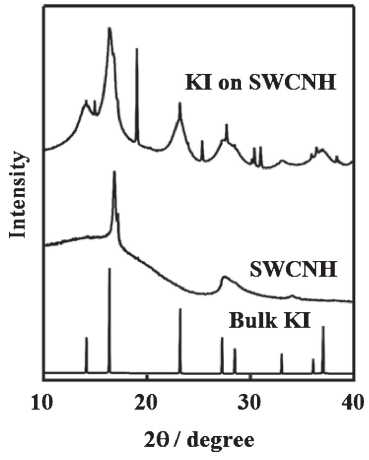

Figure 5. Synchrotron XRD patterns of SWCNH, KI on SWCNH, and bulk KI at room temperature.

Catalytic research showed that SWCNHs are excellent as the catalyst support for water formation reaction from H_2 and O_2 and also H_2 and nanotube formation reaction from CH_4.[41,42] It is probable that the excellent catalyst support of SWCNH is associated with the above superhigh-pressure effect.

♦ 4. Unique Adsorption due to Collective Interaction

The collective interaction between molecules and pores induce new adsorption phenomena described below.

4.1 Accommodative Filling of Water Molecules in Hydrophobic Spaces.

When we place a water droplet on a compressed disk plate of hydrophobic ACF, the water droplet forms a stable hemisphere. This indicates that the contact angle of water on the

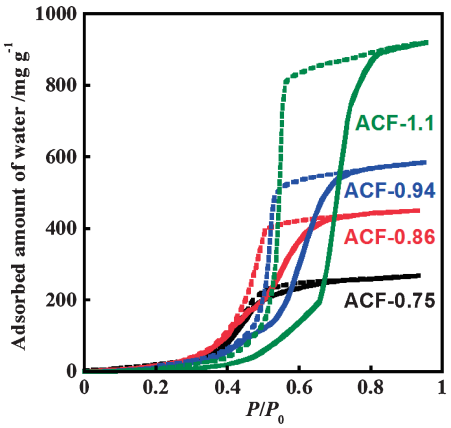

Figure 6. Water adsorption isotherms of ACFs at 303 K. Here (*X*) in ACF-*X* means the average pore width in nm.

ACF-packed surface is near 90°, being rather hydrophobic. The water vapor begins to be adsorbed suddenly on nanoporous carbons with few surface oxygen groups and hydrophobic zeolites such as $AlPO_4$-5.[43–46] Figure 6 shows water vapor adsorption isotherms of pitch-based ACFs having different pore widths from 0.75 to 1.1 nm. The water adsorption amount below $P/P_0 = 0.1$ is almost zero. In particular, water vapor is not adsorbed below $P/P_0 = 0.4$ for ACF having wider pores of 0.86, 0.94, and 1.1 (here the figure means the average pore width in nm); the adsorption begins almost vertically with increasing pore width, accompanying an evident hysteresis. On the other hand, the adsorption isotherm of ACF with the smallest micropores of 0.75 nm has a gradual increase in adsorption around $P/P_0 = 0.2$ without a clear hysteresis. In the case of $AlPO_4$-5, a vertical uptake is observed around $P/P_0 = 0.3$ without an explicit hysteresis.[46] Thus, we have several questions about water vapor adsorption on the hydrophobic nanoporous solids: What is adsorption hysteresis? Why does hydrophobic porous carbon exhibit hydrophilic behavior? Both questions should be associated with each other. The change in the adsorption hysteresis loop was examined on ACF at 303–323 K at different equilibration times of 5 min to 15 h for each measuring point.[47] Here we introduce $P_{ad1/2}$ and $P_{des1/2}$ corresponding to a half saturated adsorption amount on adsorption and desorption branches at each equilibration time, respectively, as shown in Figure 7. The $P_{ad1/2}$ decreases rapidly with time, whereas only slight decrease of $P_{des1/2}$ is observed. The difference between $P_{des1/2}$ and $P_{ad1/2}$ gives the breadth of the adsorption hysteresis loop. Figure 8 indicates that the width of the adsorption hysteresis loop decreases with the equilibration time, as shown in Figure 8. Then an adsorption branch stems from the metastable state, and the adsorption hysteresis loop disappears if we wait for a long time (a few thousand years). The energy of the metastable state should be quite close to that of the adsorbed state in the equilibrium. This indicates a structural similarity of adsorbed water molecules in the metastable and equilibrium states.

Interwater molecular interaction, that is hydrogen bonding, is crucial in water adsorption in hydrophobic pores. Ohba et al. clearly showed that cluster formation of water molecules is the reason why water molecules can adapt to hydrophobic pores.[48]

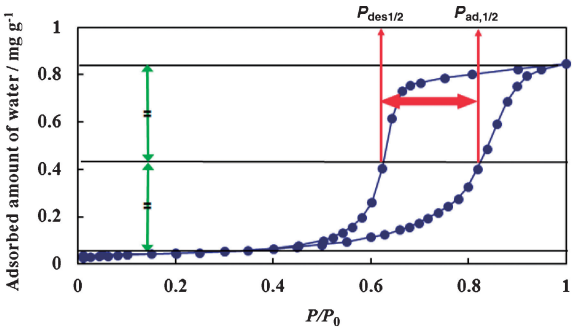

Figure 7. Definition of $P_{ad1/2}$ and $P_{des1/2}$ and breadth of adsorption hysteresis loop.

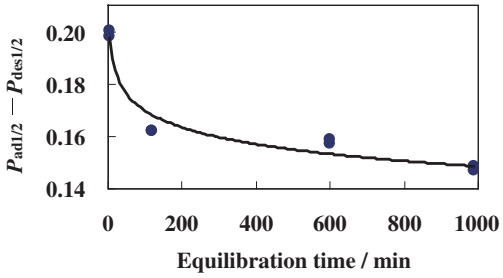

Figure 8. Relationship between half-width of hysteresis loop and equilibration time.

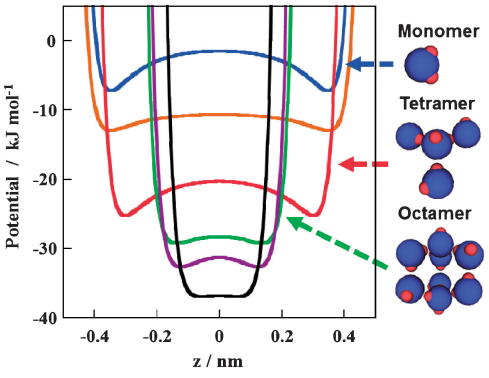

Figure 9. Total potential profiles for water molecular clusters in the slit-shaped hydrophobic carbon pore. Dimer, decamer, and dodecamer are denoted by light brown, purple, and black, respectively.

Figure 9 shows total potential profiles for water molecular clusters in the slit-shaped hydrophobic pore. Here, only highly symmetric clusters were used for evaluation of the total interaction potential which is the sum of both molecule–molecule and molecule–wall interactions per a molecule. Once clusters are formed, a water molecule in the pore obtains the large stability. The cluster formation process should be associated with the adsorption hysteresis.

The water cluster structure can be studied with in situ small-angle X-ray scattering (SAXS). The density fluctuation from SAXS is associated with cluster distribution in the pore.[49] The density fluctuation against fractional filling shows hysteresis corresponding to adsorption hysteresis. Consequently, adsorbed

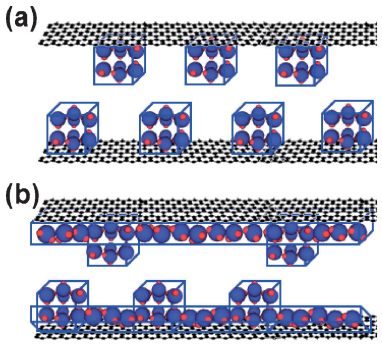

Figure 10. The adsorbed structure models on adsorption and desorption at fractional filling = 0.4.

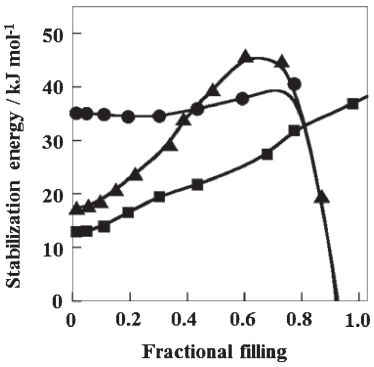

Figure 11. The stabilization energy profile with the increase of fractional filling for a 1.1 nm-width slit-shaped pore of three elementary adsorbed structures; uniform distribution structure (square), monolayer (triangle), and clusters (circle).

water structures on adsorption and desorption are different from each other. The adsorbed structure models on adsorption and desorption at fractional filling = 0.4 are shown in Figure 10. Water molecular clusters of 0.4 nm^3 are distributed in the pore during adsorption, as shown in Figure 10a. On the other hand, clusters and monolayer coexist in the pore on desorption. The energy difference between the two adsorbed models should be small, indicating that the observed metastable state is highly stable. Water molecules should form the inherent adsorbed structure relating to the metastable structure.

Iiyama et al. showed that water in the pores is not liquid, but solid-like by in situ X-ray diffraction.[50] Futamura et al. showed that adsorbed water has a cubic ice-like structure.[51] The reason why the adsorption process passes though the metastable state has been recently shown by stabilization energy calculation and molecular dynamics.[52] We assumed three elementary adsorbed structures of monolayer, associated clusters, and a uniformly hydrogen-bonded network. Figure 11 shows the stabilization energy profile of three elementary adsorbed structures with the fractional filling for slit-shaped pores of 1.1 nm in width. On adsorption, adsorption begins on the route of the cluster formation because of the greatest stabilization energy. The energy profile predicts the transfer from the cluster formation route to monolayer at fractional filling = 0.4. However, molecular dynamics provides evidence that the cluster to monolayer transformation is kinetically prohibited. Consequently, growth of clusters continues up to fractional filling of 0.8, where the transformation from the cluster to uniformly hydrogen-bonded network structures occurs. Thus, the cluster structure fractional filling of 0.4 to 0.8 is metastable. Desorption proceeds via the uniformly hydrogen-bonded network structure down to fractional filling of 0.8, where the hydrogen-bonded network route transforms to the monolayer structure of the greatest stability. Thus, the adsorption hysteresis is interpreted. This approach can give a reasonable understanding of the fact that small pores of 0.7 nm give almost no adsorption hysteresis. Apparent hydrophilicity is also given to SWCNT and DWCNT having smaller diameter.[53,54] These must be studied using the above approach in the future.

4.2 Filling of Molecular Quanta.

Adsorption of gases on solids at very low temperature often shows unusual features. The BET analysis of the He adsorption isotherm on nonporous carbon black at 4.2 K leads to nearly twice the BET surface area determined from N_2 adsorption isotherm at 77 K. Steele showed the accelerated bilayer adsorption mechanism of He at 4.2 K theoretically;[55] the partition number of He to the second layer is comparable to that of the monolayer at 4.2 K, and then the bilayer adsorption occurs almost simultaneously together with the monolayer adsorption. Adsorption of He and H_2 on the basal plane of graphite has attracted great attention with relevance to phase diagrams of quantum monolayer in low-temperature physics.[56]

Kaneko et al. studied ultramicroporosimetry with He adsorption at 4.2 K in comparison with N_2 adsorption at 77 K.[57] The collision diameter of He is 0.20 nm, being smaller than N_2. Furthermore, He has no quadrupole moment, whereas N_2 has a quadrupole moment which interacts with the polar sites on the pore wall through electrostatic interaction, giving rise to serious diffusion restriction in the ultramicropores. Consequently, He adsorption at 4.2 K has an advantage for ultramicroporosimetry compared with N_2 adsorption. He adsorption at 4.2 K provides a clearer pore size distribution than N_2 for microporous carbon. However, He is not adsorbed sufficiently on ultramicroporous carbons at 4.2 K. As ultramicroporous carbon has slit-shaped pores with width less than 0.7 nm, the translational motion of He is quantized, and a considerably large number of He atoms are excited to higher energy levels, leading to an effectively large molecular size. Therefore, He should exhibit quantum behavior in adsorption in ultramicropores at 4.2 K.[58] Theoretical physicist Beenakker et al. proposed a new concept of quantum molecular sieving for hydrogen isotopes on a cylindrical pore using a simple deep potential well model.[59] Johnson et al. have established the quantum molecular sieving mechanism with quantum simulation using Feynman–Hibbs (FH) potential approximation and rigorous path integral (PI) approximation.[60] Here, the path integral method is applicable to adsorption even at 4.2 K, whereas the FH potential can be applicable to adsorption above about 40 K.[61] Figure 12 shows the interaction potential profiles of classical H_2 (D_2), quantum H_2, and quantum D_2 with SWCNT, which are calculated with the FH potential at 20 K, although the FH approximation is not appropriate compared with the PI method. Here, the FH potential is given by eq 2. Ordinarily, the quadratic form has been used for the FH simulation.

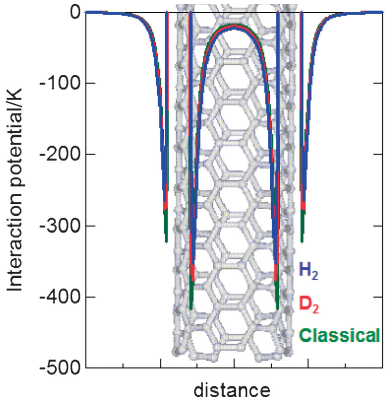

Figure 12. Interaction potential profiles of classical H_2 (D_2), quantum H_2, and quantum D_2 with SWCNT (diameter = 3 nm).

$$V_{FH}(r) = V_{LJ}(r) + \frac{\hbar^2}{24\mu kT}\left(V''_{LJ}(r) + \frac{2}{r}V'_{LJ}(r)\right) \quad (2)$$

V_{LJ}: Classical LJ pair potential

μ: Reduced mass of a pair of particles ($= M/2$)

M: Molecular mass

T: Temperature

As the LJ potentials for H_2 and D_2 are identical, we cannot distinguish H_2 and D_2 with a theoretical approach using the LJ potential. On the other hand, the FH potential contains the mass of a molecule and the adsorption temperature, and thereby the different adsorption behavior of H_2 and D_2 can be predicted, as shown in Figure 12. The heavier the mass of the hydrogen isotope, the deeper the potential well and the smaller the potential minimum distance become. Therefore, H_2 molecules more weakly interact than D_2, and the effective size of H_2 is larger than that of D_2. On the contrary, classical H_2 or D_2 gives the deepest potential minimum and the smallest potential minimum distance. SWCNT has both the internal tube wall having negative curvature and the external tube wall having positive curvature. As the radius of the curvature is a nanometer scale, the potential profile difference is really marked; the potential minimum difference of 100 Kk_B is about one third of the potential minimum value for the external wall. Therefore, adsorption behavior of H_2 and D_2 greatly depends on the sign of the curvature of the tube wall. The above-mentioned potential difference of H_2 and D_2 has been expected to provide a superhigh selectivity of SWCNT for H_2 and D_2 theoretically.[60] The selectivity $S(D_2/H_2)$ is given by the adsorption amount and gas phase concentration of H_2 and D_2, as follows.

$$S(D_2/H_2) = \frac{x_{D_2}/x_{H_2}}{y_{D_2}/y_{H_2}} \quad (3)$$

Here, x_{D_2} and x_{H_2} are the adsorption amounts of D_2 and H_2, respectively; y_{D_2} and y_{H_2} are the gas-phase concentrations of D_2 and H_2, respectively. However, no direct study has been reported supporting the theoretical prediction of quantum molecular sieving before the work on SWCNH by Tanaka et al.[62] They measured adsorption isotherms of H_2 and D_2 on open and closed SWCNHs at 40 and 77 K. The adsorption amount of D_2 is larger than that of H_2 at 40 K by 10%. The difference decreases with the elevation of the measuring temperature. They simulated

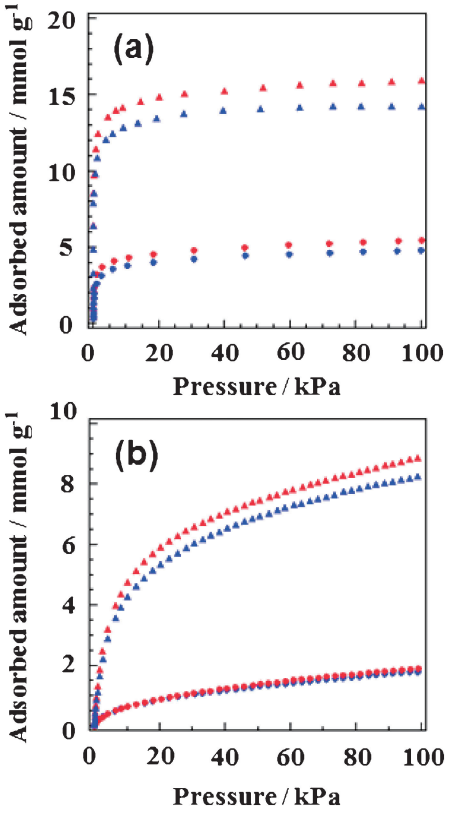

Figure 13. H_2 and D_2 isotherms on open and closed SWCNT at (a) 40 and (b) 77 K; D_2 on open SWCNT (▲), H_2 on open SWCNT (▲), D_2 on closed SWCNT (●), and H_2 on closed SWCNT (●).

adsorption isotherms of H_2 and D_2 in the internal tube spaces at 77 K using the FH potential, agreeing with the experimental isotherms. As the classical potential cannot simulate the experimental isotherms, the quantum molecular sieving effect is explicitly evidenced. They gave similar results on activated carbon fiber, $AlPO_4$-5, Cu-based PCP, and SWCNT,[63–66] although they predicted the adsorption selectivity using the adsorption isotherms of pure H_2 and D_2. This quantum molecular sieving effect is a general phenomenon, being observable on various nanoporous solids.

Figure 13 shows the adsorption isotherms of H_2 and D_2 on SWCNT at 40 and 77 K. The experimental $S(D_2/H_2)$ at 40 K and 10^{-5}–10^{-3} MPa is 2.8 using the ideal adsorbed solution theory (IAST).[67] This observed value is close to the quantum simulated $S(D_2/H_2)$. However, ordinary simulation gives a much larger $S(D_2/H_2)$ than the observed value, because grand canonical Monte Carlo simulation has no pore blocking effect, but the correct measurement of an experimental isotherm in the equilibrium is always difficult. Very recently adsorption isotherms of H_2 and D_2 on pore-structure-controlled SWCNTs were measured at 20–77 K. We used SG-SWCNTs.[6] The SG-SWCNTs do not form the bundle structure. Drying the SG-SWCNT after dipping in toluene provides the fine bundle structure which has interstitial pores of 0.5 nm in width.[68] This bundled SWCNT gives a relatively large $S(D_2/H_2)$ value compared with individual SWCNTs.[69] Fujimori et al. designed a mixed gas adsorption measuring system at low temperature. They measured $S(D_2/H_2)$

for ACFs having different pore widths of 0.7 to 1.2 nm, carbon molecular sieves, and zeolites at 77 K. $S(D_2/H_2)$ for ACFs are about 1.7–1.8, being independent of the pore width, and both carbon molecular sieve and zeolites give a larger $S(D_2/H_2)$ value of 2.[70] The $S(D_2/H_2)$ values are still smaller than the simulation values, of which the reason must be studied in the future. Recent studies on methane isotope mixture such as $^{12}CH_4$ and $^{12}CD_4$, and $^{12}CH_4$ and $^{13}CH_4$ show astonishing results that even methane isotopes can be separable with the quantum molecular sieving effect.[71]

4.3 Surface Adsorption-initiating Gate Adsorption.

$[Cu(bpy)_2(H_2O)_2(BF_4)_2]$ is easily synthesized in the form of crystals of sub-mm scales. The crystal has a layer structure which has rectangular voids. However, these layers are stacked with the shift of a half of the lattice constant, and thereby this crystal has no open pores. Consequently, vapor molecules should be adsorbed only on the external surface of the crystals. However, unexpected adsorption was found for CO_2 after the dehydration of $[Cu(bpy)_2(H_2O)_2(BF_4)_2]$. CO_2 is not adsorbed up to the threshold pressure (gate adsorption pressure) $P_{g,a}$, but a vertical adsorption occurs at the gate pressure, becoming almost a plateau above the CO_2 pressure. This adsorption isotherm is just like a step-function. During desorption, adsorbed CO_2 evaporates at the desorption gate pressure $P_{g,d}$, which is smaller than $P_{g,a}$. The adsorption amount at $P_{g,a}$ is nearly equal to the total void volume in the layer structures. This indicates the continuous bridging of isolated voids in the neighboring layers. This adsorption was named "gate adsorption." The gate adsorption is highly reproducible, as shown in Figure 14. Accordingly this crystal aspires CO_2 with a structural change.[72] Synchrotron X-ray diffraction clearly shows that the *c* axis of the $[Cu(bpy)_2(BF_4)_2]$ expands by 27% on adsorption of CO_2 and that it recovers on desorption. The expansion and shrinkage of the crystal lattice by 27% occurs repeatedly in maintaining the crystal structure.[73] This phenomenon gives a new aspect on solid which should not vary the structure in response to external stimuli. Later a similar flexibility was observed in another PCP crystal MIL-53: In the case of MIL-53, the crystal has intrinsic pore structure of which shape varies on adsorption.[74] This adsorption behavior is called "breathing effect."

The $[Cu(bpy)_2(H_2O)_2(BF_4)_2]$ crystals must be dehydrated to induce the gate adsorption. The dehydrated $[Cu(bpy)_2(BF_4)_2]$ is denoted ELM-11 (elastic-layer-structured metal organic framework (ELM)). Similar gate adsorption is observed for CH_4, N_2, and O_2, although the gate adsorption is not critical like CO_2 adsorption. Ni- and Co-based layered PCPs as well as ELM-11 $[Cu(bpy)_2(BF_4)_2]$ exhibit similar gate adsorption.[75] Two-step adsorption isotherms are observed for N_2, CO_2, and Ar on $[Cu(bpy)_2(OTf)_2]$.[76] Although the crystal structure of ordinary PCP crystals partially collapses on water vapor adsorption, $[Cu(bpy)_2(H_2O)_2(BF_4)_2]$ is highly resistive for exposure to water vapor.

The dehydrated $[Cu(bpy)_2(BF_4)_2]$ has a pillar-frame porous structure highly sensitive to the surroundings, and thereby the adsorbed state on the surface governs the total stabilization energy. This is the principal cause for the gate adsorption accompanying the lattice structural change. Recently, synchrotron X-ray diffraction showed that a weak peak corresponding to the *d* spacing of 0.93 nm appears at 27 kPa below the gate adsorption pressure of 32 kPa.[77] Probably this is a key forerunning step for the collective gate adsorption. This gate adsorption due to dramatic lattice flexibility is promising for energy-saving separation.

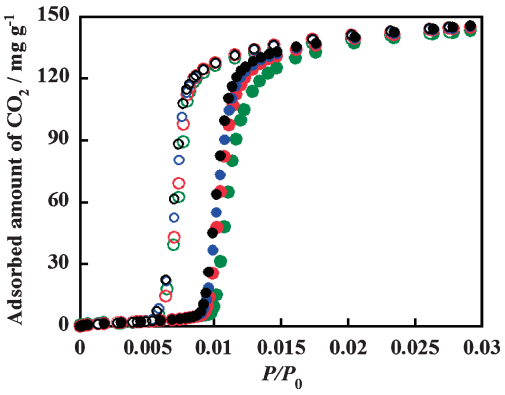

Figure 14. Reproducible CO_2 gate adsorption of $[Cu(bpy)_2(BF_4)_2]$ at 273 K; 1st run (green), 2nd run (red), 3rd run (blue), and 4th run (black).

♦ *5. Conclusion: Nanoconfined Electrolytes, Defective Nanostructures, and Future Perspectives*

As interfacial solids have huge surface area, adsorbed molecules affect the total energy of the solid significantly. The representative adsorption features inherent to interfacial solids are shown in this article. We hope for further development of collective-interaction-induced adsorption. The residual example is adsorption of ions in the pore spaces. As we need to take into account the electrostatic interaction of long-range order to understand the state and properties of ionic molecules, we can expect unusual features of ionic molecules in the nanoscale pore spaces. EXAFS study showed the partial dehydration of Rb^+ in the slit and tube spaces; apparent hydration numbers are around 5.3 in the slit pore and 2.6 in the tube pore.[78,79] This gives new insight into ionic solution chemistry. Also, confinement of organic electrolyte solution in the slit-shaped pores induces an unusually oriented structure of ionic molecules.[80] The confined electrolytic solution is associated with the fundamentals of a supercapacitor which is a representative eco-device. Thus, the study of confined electrolytic solutions should directly contribute to technological development. Further studies on collective interaction between molecules or ions and interfacial solids are indispensable to construct new sustainable technology as well as to establish new interface chemistry. As SWCNT and SWCNH have dynamic nature through pentagon–heptagon morphological defects and both graphite nanoribbon and graphene belts have edge-rich structures,[41,42,81–83] which are predicted to induce unusual chemical activities, new types of the collective interactions of molecules with new interfacial solids should be observed in the future.

K. K., T. I., and T. F. have been supported by Exotic Nanocarbons, Japan Regional Innovation Strategy Program by the Excellence, JST. This work has been supported by Grant-in-Aids for Fundamental Scientific Research (S) (Grant

No. 15101003) and (A) (Grant No. 21241026) and the Strategic Promotion Program for Basic Nuclear Research by MEXT. Dr. H. Tanaka (Kyoto University), Dr. K. Urita (Nagasaki University), and Dr. T. Ohba (Chiba University) supported potential calculation and drawing figures in part.

References and Notes

1 Y. Tao, H. Kanoh, L. Abrams, K. Kaneko, *Chem. Rev.* **2006**, *106*, 896.
2 S. Lei, J.-i. Miyamoto, H. Kanoh, Y. Nakahigashi, K. Kaneko, *Carbon* **2006**, *44*, 1884.
3 a) T. Yanagisawa, T. Shimizu, K. Kuroda, C. Kato, *Bull. Chem. Soc. Jpn.* **1990**, *63*, 988. b) S. Iijima, *Nature* **1991**, *354*, 56. c) C. T. Kresge, M. E. Leonowicz, W. J. Roth, J. C. Vartuli, J. S. Beck, *Nature* **1992**, *359*, 710. d) S. Iijima, T. Ichihashi, *Nature* **1993**, *363*, 603. e) D. S. Bethune, C. H. Klang, M. S. de Vries, G. Gorman, R. Savoy, J. Vazquez, R. Beyers, *Nature* **1993**, *363*, 605.
4 K. Ariga, A. Vinu, Y. Yamauchi, Q. Ji, J. P. Hill, *Bull. Chem. Soc. Jpn.* **2012**, *85*, 1.
5 S. Iijima, M. Yudasaka, R. Yamada, S. Bandow, K. Suenaga, F. Kokai, K. Takahashi, *Chem. Phys. Lett.* **1999**, *309*, 165.
6 K. Hata, D. N. Futaba, K. Mizuno, T. Namai, M. Yumura, S. Iijima, *Science* **2004**, *306*, 1362.
7 M. O'Keeffe, O. M. Yaghi, *Chem. Rev.* **2012**, *112*, 675.
8 F.-X. Coudert, A. Boutin, M. Jeffroy, C. Mellot-Draznieks, A. H. Fuchs, *ChemPhysChem* **2011**, *12*, 247.
9 T. Uemura, N. Yanai, S. Kitagawa, *Chem. Soc. Rev.* **2009**, *38*, 1228.
10 G. Férey, *Chem. Soc. Rev.* **2008**, *37*, 191.
11 M. Endo, T. Hayashi, H. Muramatsu, Y.-A. Kim, H. Terrones, M. Terrones, M. S. Dresselhaus, *Nano Lett.* **2004**, *4*, 1451.
12 H. Kataura, Y. Kumazawa, Y. Maniwa, I. Umezu, S. Suzuki, Y. Ohtsuka, Y. Achiba, *Synth. Met.* **1999**, *103*, 2555.
13 T. Ohba, K. Murata, K. Kaneko, W. A. Steele, F. Kokai, K. Takahashi, D. Kasuya, M. Yudasaka, S. Iijima, *Nano Lett.* **2001**, *1*, 371.
14 M. Arai, S. Utsumi, M. Kanamaru, K. Urita, T. Fujimori, N. Yoshizawa, D. Noguchi, K. Nishiyama, Y. Hattori, F. Okino, T. Ohba, H. Tanaka, H. Kanoh, K. Kaneko, *Nano Lett.* **2009**, *9*, 3694.
15 a) E. A. Guggenheim, *Mol. Phys.* **1966**, *10*, 401. b) C. E. Dinerman, G. E. Ewing, *J. Chem. Phys.* **1970**, *53*, 626.
16 K. Kaneko, N. Fukuzaki, S. Ozeki, *J. Chem. Phys.* **1987**, *87*, 776.
17 K. Kaneko, N. Fukuzaki, K. Kakei, T. Suzuki, S. Ozeki, *Langmuir* **1989**, *5*, 960.
18 H. Uchiyama, S. Ozeki, K. Kaneko, *Chem. Phys. Lett.* **1990**, *166*, 531.
19 O. Byl, P. Kondratyuk, J. T. Yates, Jr., *J. Phys. Chem. B* **2003**, *107*, 4277.
20 a) K. Nishikawa, K. Tohji, Y. Murata, *J. Chem. Phys.* **1981**, *74*, 5817. b) J. Ll. Tamarit, M. Barrio, L. C. Pardo, P. Negrier, D. Mondieig, *J. Phys.: Condens. Matter* **2008**, *20*, 244110. c) E. J. Valente, L. S. Bartell, *J. Chem. Phys.* **1984**, *80*, 1458.
21 T. Iiyama, K. Nishikawa, T. Suzuki, T. Otowa, M. Hijiriyama, Y. Nojima, K. Kaneko, *J. Phys. Chem. B* **1997**, *101*, 3037.
22 M. Miyahara, K. E. Gubbins, *J. Chem. Phys.* **1997**, *106*, 2865.
23 A. Watanabe, T. Iiyama, K. Kaneko, *Chem. Phys. Lett.* **1999**, *305*, 71.
24 K. Kaneko, A. Watanabe, T. Iiyama, R. Radhakrishan, K. E. Gubbins, *J. Phys. Chem. B* **1999**, *103*, 7061.
25 R. Radhakrishnan, K. E. Gubbins, A. Watanabe, K. Kaneko, *J. Chem. Phys.* **1999**, *111*, 9058.
26 S. Hashimoto, T. Fujimori, H. Tanaka, K. Urita, T. Ohba, H. Kanoh, T. Itoh, M. Asai, H. Sakamoto, S. Niimura, M. Endo, F. Rodriguez-Reinoso, K. Kaneko, *J. Am. Chem. Soc.* **2011**, *133*, 2022.
27 L. D. Gelb, K. E. Gubbins, R. Radhakrishnan, M. Śliwinska-Bartkowiak, *Rep. Prog. Phys.* **1999**, *62*, 1573.
28 a) H. Kanda, M. Miyahara, *J. Chem. Phys.* **2007**, *126*, 54703. b) H. Kanda, M. Miyahara, *Adsorption* **2007**, *13*, 191.
29 S. F. Agnew, B. I. Swanson, L. H. Jones, R. L. Mills, *J. Phys. Chem.* **1985**, *89*, 1678.
30 J. Imai, M. Souma, S. Ozeki, T. Suzuki, K. Kaneko, *J. Phys. Chem.* **1991**, *95*, 9955.
31 Y. Nishi, T. Suzuki, K. Kaneko, *J. Phys. Chem.* **1997**, *101*, 1938.
32 M. Iwamoto, H. Furukawa, Y. Mine, F. Uemura, S.-i. Mikuriya, S. Kagawa, *J. Chem. Soc., Chem. Commun.* **1986**, 1272.
33 T. Yamamoto, D. A. Tryk, K. Hashimoto, A. Fujishima, M. Okawa, *J. Electrochem. Soc.* **2000**, *147*, 3393.
34 K. Hara, A. Kudo, T. Sakata, M. Watanabe, *J. Electrochem. Soc.* **1995**, *142*, L57.
35 E. E. Santiso, A. M. George, K. E. Gubbins, M. B. Nardelli, *J. Chem. Phys.* **2006**, *125*, 084711.
36 Y. Long, J. C. Palmer, B. Coasne, M. Śliwinska-Bartkowiak, K. E. Gubbins, *Phys. Chem. Chem. Phys.* **2011**, *13*, 17163.
37 K. Asaumi, T. Mori, *Phys. Rev. B* **1983**, *28*, 3529.
38 R. R. Meyer, J. Sloan, R. E. Dunin-Borkowski, A. I. Kirkland, M. C. Novotny, S. R. Bailey, J. L. Hutchison, M. L. H. Green, *Science* **2000**, *289*, 1324.
39 K. Urita, Y. Shiga, T. Fujimori, T. Iiyama, Y. Hattori, H. Kanoh, T. Ohba, H. Tanaka, M. Yudasaka, S. Iijima, I. Moriguchi, F. Okino, M. Endo, K. Kaneko, *J. Am. Chem. Soc.* **2011**, *133*, 10344.
40 Unpublished.
41 T. Itoh, H. Danjo, W. Sasaki, K. Urita, E. Bekyarova, M. Arai, T. Imamoto, M. Yudasaka, S. Iijima, H. Kanoh, K. Kaneko, *Carbon* **2008**, *46*, 172.
42 a) Y. Aoki, K. Urita, D. Noguchi, T. Itoh, H. Kanoh, T. Ohba, M. Yudasaka, S. Iijima, K. Kaneko, *Chem. Phys. Lett.* **2009**, *482*, 269. b) S. Wang, T. Itoh, T. Fujimori, M. Castro, A. M. Silvestre-Albero, F. Rodríguez-Reinoso, T. Ohba, H. Kanoh, K. Kaneko, *Langmuir*, Just Accepted Manuscript. doi:10.1021/la3006986.
43 J. Miyawaki, T. Kanda, K. Kaneko, *Langmuir* **2001**, *17*, 664.
44 D. Mowla, D. D. Do, K. Kaneko, in *Chemistry and Physics of Carbon*, ed. by L. R. Radovic, Marcel Dekker, Inc., New York, **2003**, Vol. 28, pp. 229–262.
45 A. Striolo, *Adsorpt. Sci. Technol.* **2011**, *29*, 211.
46 N. Floquet, J. P. Coulomb, N. Dufau, G. Andre, R. Kahn, *Adsorption* **2005**, *11*, 139.
47 M. Nakamura, T. Ohba, P. Branton, H. Kanoh, K. Kaneko,

Carbon **2010**, *48*, 305.
48 T. Ohba, H. Kanoh, K. Kaneko, *J. Am. Chem. Soc.* **2004**, *126*, 1560.
49 T. Ohba, H. Kanoh, K. Kaneko, *Nano Lett.* **2005**, *5*, 227.
50 a) T. Iiyama, K. Nishikawa, T. Otowa, K. Kaneko, *J. Phys. Chem.* **1995**, *99*, 10075. b) M.-C. Bellissent-Funel, R. Sridi-Dorbez, L. Bosio, *J. Chem. Phys.* **1996**, *104*, 10023.
51 R. Futamura, T. Iiyama, A. Hamasaki, S. Ozeki, *Phys. Chem. Chem. Phys.* **2012**, *14*, 981.
52 T. Ohba, K. Kaneko, *Langmuir* **2011**, *27*, 7609.
53 Y. Tao, H. Muramatsu, M. Endo, K. Kaneko, *J. Am. Chem. Soc.* **2010**, *132*, 1214.
54 H.-J. Wang, X.-K. Xi, A. Kleinhammes, Y. Wu, *Science* **2008**, *322*, 80.
55 W. A. Steele, *J. Chem. Phys.* **1956**, *25*, 819.
56 a) L. W. Bruch, M. W. Cole, E. Zaremba, *Physical Adsorption: Forces and Phenomena*, Oxford University Press, Oxford, **1997**, Chap. 6. b) P. Kowalczyk, P. A. Gauden, A. P. Terzyk, S. Furmaniak, K. Kaneko, *J. Phys. Chem. C* **2011**, *115*, 18105.
57 a) N. Setoyama, K. Kaneko, *Adsorption* **1995**, *1*, 165. b) N. Setoyama, K. Kaneko, F. Rodríguez-Reinoso, *J. Phys. Chem.* **1996**, *100*, 10331.
58 K. Kaneko, N. Setoyama, T. Suzuki, *Stud. Surf. Sci. Catal.* **1994**, *87*, 593.
59 J. J. M. Beenakker, V. D. Borman, S. Yu. Krylov, *Chem. Phys. Lett.* **1995**, *232*, 379.
60 a) Q. Wang, J. K. Johnson, J. Q. Broughton, *J. Chem. Phys.* **1997**, *107*, 5108. b) Q. Wang, S. R. Challa, D. S. Sholl, J. K. Johnson, *Phys. Rev. Lett.* **1999**, *82*, 956. c) S. R. Challa, D. S. Sholl, J. K. Johnson, *J. Chem. Phys.* **2002**, *116*, 814. d) G. Garberoglio, J. K. Johnson, *ACS Nano* **2010**, *4*, 1703.
61 a) L. M. Sesé, *Mol. Phys.* **1995**, *85*, 931. b) G. Stan, M. W. Cole, *J. Low Temp. Phys.* **1998**, *110*, 539.
62 H. Tanaka, H. Kanoh, M. Yudasaka, S. Iijima, K. Kaneko, *J. Am. Chem. Soc.* **2005**, *127*, 7511.
63 Y. Hattori, H. Tanaka, F. Okino, H. Touhara, Y. Nakahigashi, S. Utsumi, H. Kanoh, K. Kaneko, *J. Phys. Chem. B* **2006**, *110*, 9764.
64 H. Tanaka, D. Noguchi, A. Yuzawa, T. Kodaira, H. Kanoh, K. Kaneko, *J. Low Temp. Phys.* **2009**, *157*, 352.
65 D. Noguchi, H. Tanaka, A. Kondo, H. Kajiro, H. Noguchi, T. Ohba, H. Kanoh, K. Kaneko, *J. Am. Chem. Soc.* **2008**, *130*, 6367.
66 D. Noguchi, H. Tanaka, T. Fujimori, H. Kagita, Y. Hattori, H. Honda, K. Urita, S. Utsumi, Z.-M. Wang, T. Ohba, H. Kanoh, K. Hata, K. Kaneko, *J. Phys.: Condens. Matter* **2010**, *22*, 334207.
67 A. L. Myers, J. M. Prausnitz, *AIChE J.* **1965**, *11*, 121.
68 M. Yamamoto, T. Itoh, H. Sakamoto, T. Fujimori, K. Urita, Y. Hattori, T. Ohba, H. Kagita, H. Kanoh, S. Niimura, K. Hata, K. Takeuchi, M. Endo, F. Rodríguez-Reinoso, K. Kaneko, *Adsorption* **2011**, *17*, 643.
69 H. Kagita, T. Ohba, T. Fujimori, Y. Hattori, H. Kanoh, H. Tanaka, T. Itoh, K. Hata, S. Taira, D. Minami, M. Endo, K. Kaneko, to be submitted.
70 S. Niimura, T. Fujimori, L. Abrams, D. R. Corbin, K. Kaneko, to be submitted.
71 T. Fujimori, T. Tamura, D. Minami, S. Niimura, T. Ohba, T. Itoh, H. Kanoh, K. Kaneko, in preparation.
72 S. Onishi, T. Ohmori, T. Ohkubo, H. Noguchi, L. Di, Y. Hanzawa, H. Kanoh, K. Kaneko, *Appl. Surf. Sci.* **2002**, *196*, 81.
73 A. Kondo, H. Noguchi, S. Ohnishi, H. Kajiro, A. Tohdoh, Y. Hattori, W.-C. Xu, H. Tanaka, H. Kanoh, K. Kaneko, *Nano Lett.* **2006**, *6*, 2581.
74 C. Serre, S. Bourrelly, A. Vimont, N. A. Ramsahye, G. Maurin, P. L. Llewellyn, M. Daturi, Y. Filinchuk, O. Leynaud, P. Barnes, G. Férey, *Adv. Mater.* **2007**, *19*, 2246.
75 H. Kajiro, A. Kondo, K. Kaneko, H. Kanoh, *Int. J. Mol. Sci.* **2010**, *11*, 3803.
76 A. Kondo, H. Kajiro, H. Noguchi, L. Carlucci, D. M. Proserpio, G. Ciani, K. Kato, M. Takata, H. Seki, M. Sakamoto, Y. Hattori, F. Okino, K. Maeda, T. Ohba, K. Kaneko, H. Kanoh, *J. Am. Chem. Soc.* **2011**, *133*, 10512.
77 A. Kondo, N. Kojima, H. Kajiro, H. Noguchi, Y. Hattori, F. Okino, K. Maeda, T. Ohba, K. Kaneko, H. Kanoh, *J. Phys. Chem. C* **2012**, *116*, 4157.
78 T. Ohkubo, T. Konishi, Y. Hattori, H. Kanoh, T. Fujikawa, K. Kaneko, *J. Am. Chem. Soc.* **2002**, *124*, 11860.
79 T. Ohkubo, Y. Hattori, H. Kanoh, T. Konishi, H. Sakai, M. Abe, D. Kasuya, M. Yudasaka, S. Iijima, T. Fujikawa, K. Kaneko, *Phys. Scr.* **2005**, 685.
80 A. Tanaka, T. Iiyama, T. Ohba, S. Ozeki, K. Urita, T. Fujimori, H. Kanoh, K. Kaneko, *J. Am. Chem. Soc.* **2010**, *132*, 2112.
81 a) T. Fujimori, K. Urita, T. Ohba, H. Kanoh, K. Kaneko, *J. Am. Chem. Soc.* **2010**, *132*, 6764. b) T. Fujimori, K. Urita, D. Tománek, T. Ohba, I. Moriguchi, M. Endo, K. Kaneko, *J. Chem. Phys.* **2012**, *136*, 64505. c) T. Fujimori, L. R. Radovic, A. B. Silva-Tapia, M. Endo, K. Kaneko, *Carbon*, **2011**, in press. doi:10.1016/j.carbon.2011.12.010.
82 M. Asai, T. Ohba, T. Iwanaga, H. Kanoh, M. Endo, J. Campos-Delgado, M. Terrones, K. Nakai, K. Kaneko, *J. Am. Chem. Soc.* **2011**, *133*, 14880.
83 A. Morelos-Gómez, S. M. Vega-Díaz, V. J. González, F. Tristán-López, R. Cruz-Silva, K. Fujisawa, H. Muramatsu, T. Hayashi, X. Mi, Y. Shi, H. Sakamoto, F. Khoerunnisa, K. Kaneko, B. G. Sumpter, Y. A. Kim, V. Meunier, M. Endo, E. Muñoz-Sandoval, M. Terrones, *ACS Nano* **2012**, *6*, 2261.

